In operando-formed interface between silver and perovskite oxide for efficient electroreduction of carbon dioxide to carbon monoxide

Wu, Xinhao; Guo, Yanan; Gu, Yuxing; Xie, Fenghua; Li, Mengran; Hu, Zhiwei; Lin, Hong Ji; Pao, Chih Wen; Huang, Yu Cheng; More Authors

Important note
To cite this publication, please use the final published version (if applicable).
Please check the document version above.

RESEARCH ARTICLE

CARBON ENERGY WILEY

In operando-formed interface between silver and perovskite oxide for efficient electroreduction of carbon dioxide to carbon monoxide

Xinhao Wu[1] | Yanan Guo[1] | Yuxing Gu[1] | Fenghua Xie[1] | Mengran Li[2] | Zhiwei Hu[3] | Hong-Ji Lin[4] | Chih-Wen Pao[4] | Yu-Cheng Huang[5] | Chung-Li Dong[6] | Vanessa K. Peterson[7] | Ran Ran[1] | Wei Zhou[1] | Zongping Shao[1,8]

[1]State Key Laboratory of Materials-Oriented Chemical Engineering | College of Chemical Engineering, Nanjing Tech University, Nanjing, Jiangsu, China

[2]Department of Chemical Engineering, Materials for Energy Conversion and Storage (MECS), Faculty of Applied Sciences, Delft University of Technology, HZ Delft, The Netherlands

[3]Max Planck Institute for Chemical Physics of Solids, Dresden, Germany

[4]National Synchrotron Radiation Research Center, Hsinchu, Taiwan, China

[5]Department of Electrophysics, National Yang Ming Chiao Tung University, Hsinchu, Taiwan, China

[6]Department of Physics, Tamkang University, New Taipei City, Taiwan, China

[7]Australian Centre for Neutron Scattering, Australian Nuclear Science and Technology Organisation, Sydney, New South Wales, Australia

[8]Department of Chemical Engineering, Curtin University, Perth, Western Australia, Australia

Correspondence
Wei Zhou and Zongping Shao, State Key Laboratory of Materials-Oriented Chemical Engineering, College of Chemical Engineering, Nanjing Tech University, 211800 Nanjing, China.
Email: zhouwei1982@njtech.edu.cn and shaozp@njtech.edu.cn

Abstract

Electrochemical carbon dioxide (CO_2) reduction (ECR) is a promising technology to produce valuable fuels and feedstocks from CO_2. Despite large efforts to develop ECR catalysts, the investigation of the catalytic performance and electrochemical behavior of complex metal oxides, especially perovskite oxides, is rarely reported. Here, the inorganic perovskite oxide Ag-doped $(La_{0.8}Sr_{0.2})_{0.95}Ag_{0.05}MnO_{3-\delta}$ (LSA0.05M) is reported as an efficient electrocatalyst for ECR to CO for the first time, which exhibits a Faradaic efficiency (FE) of 84.3%, a remarkable mass activity of $75\,A\,g^{-1}$ (normalized to the mass of Ag), and stability of 130 h at a moderate overpotential of 0.79 V. The LSA0.05M catalyst experiences structure reconstruction during ECR, creating the in operando-formed interface between the perovskite and the evolved Ag phase. The evolved Ag is uniformly distributed with a small particle size on the perovskite surface. Theoretical calculations indicate the reconstruction of LSA0.05M during ECR and reveal that the perovskite–Ag interface provides adsorption sites for CO_2 and accelerates the

Xinhao Wu, Yanan Guo, and Yuxing Gu contributed equally to this study.

desorption of the *CO intermediate to enhance ECR. This study presents a novel high-performance perovskite catalyst for ECR and may inspire the future design of electrocatalysts via the in operando formation of metal–metal oxide interfaces.

KEYWORDS

electrochemical CO_2 reduction, faradaic efficiencies, interfaces, perovskite oxides

1 | INTRODUCTION

The continuous increase of CO_2 in the atmosphere due to the excessive combustion of fossil fuels has aroused general concerns about the global climate. How to capture, store, and convert atmospheric CO_2, has, therefore, become an important topic.[1–4] Electrochemical CO_2 reduction (ECR) technology, driven by renewable energy sources, offers a promising avenue for the conversion of CO_2 into valuable chemicals and fuels.[5,6] However, high overpotentials tend to be required to break the thermodynamically stable carbon–oxygen bond, leading to the low energy efficiency of the whole system.[7–9] Another challenge of ECR in aqueous solution comes from the competitive hydrogen evolution reaction (HER), which consumes cathodic electrons to produce hydrogen, degrading the ECR selectivity and overall energy efficiency.[10–14]

Enormous efforts have been devoted to developing ECR catalysts to address this challenge, and several design strategies have been proposed to guide the development of catalysts over the past decades.[15–19] It has recently been demonstrated that interface engineering can significantly improve catalytic performance[20–22] with two different components at the interface able to stabilize the key intermediate during ECR synergistically.[23,24] Constructing the metal and carbon-based interface is a simple but useful approach. For example, gold nanoparticles (AuNPs) embedded in a graphene nanoribbon (GNR) matrix exhibited improved activity, selectivity, and stability toward CO production, as a result of the AuNP–GNR interface.[25] Metal and single-metal oxide interfaces are also frequently reported in ECR.[21,26] One of our recent works designed an Ag/Ag-doped CeO_2 nanocomposite with a rich and stable three-dimensional (3D) interface for efficient CO_2 electroreduction.[20] Lee et al.[27] demonstrated that Cu–ceria interfaces could enhance the selectivity of ethylene and suppress the HER during electroreduction of CO_2. A 3D network containing metallic Cu, CeO_x nanoparticles, and carbon nanofibers (Cu/CeO_x@CNFs) was constructed by Zong et al.,[28] enabling the beneficial adsorption of the intermediates to produce CO as a result of the Cu–CeO_x interface. Apart from ceria, other metal oxides, such as

TiO_2 and In_2O_3, can also serve as supports to form metal–oxide interfaces.[11,29,30] Briefly, these interfaces are typically constructed during the preparation of catalysts, before the electrocatalytic reaction. Investigations, which involve the in operando formation of such interfaces during ECR and the utilization of complex metal oxides as supporting materials, are rarely reported.

Perovskite oxides may offer new opportunities for the in operando formation of interfaces beneficial to ECR to CO.[31–34] The A-site elements of perovskite oxides are typically alkaline earth or rare earth elements, which may promote the absorption of carbon dioxide.[35,36] Elements may exsolve from perovskite oxides into a surface cluster during ECR,[37,38] creating an interface between the evolved component and the bulk perovskite. To date, studies of perovskite oxides in ECR have mainly focused on the La_2CuO_4 catalyst. Schwartz et al.[39] pioneered research applying $La_{1.8}Sr_{0.2}CuO_4$ for ECR to alcohol. Chen et al.[38] reported an efficient La_2CuO_4 catalyst for ECR to methane, reporting the structural evolution of the perovskite during the electrochemical reaction, with theoretical calculations revealing that the formed Cu/La_2CuO_4 interface played an important role in the CO_2 methanation process.

In contrast, however, Pi et al.[40] synthesized novel $SrSnO_3$ perovskite nanowires for ECR to formate with remarkable selectivity over a broad potential window. Interestingly, the structure and composition of $SrSnO_3$ were unchanged after ECR, confirmed by ex-situ characterization.[40] More recently, they developed a nanobamboo La_2CuO_4 perovskite for ECR to ethylene and reported the stable valence of Cu in La_2CuO_4 during ECR using in situ X-ray absorption spectroscopy (XAS).[41] Substantially more effort is required to clarify both the structural stability and composition of perovskite catalysts during ECR, which is essential to guiding the development of new perovskite catalysts for efficient and selective ECR.[42–44]

Herein, we report the first study of the Ag-doped perovskite oxide $(La_{0.8}Sr_{0.2})_{0.95}Ag_{0.05}MnO_{3-\delta}$ (LSA0.05M) as an efficient electrocatalyst for ECR to CO product. Experimentally, the LSA0.05M catalyst exhibits an 84.3% Faradaic efficiency (FE) toward CO and high mass activity of 75 A g^{-1} at an overpotential of 0.79 V, coupled

with a stable operation for 130 h. The introduction of Ag into the perovskite is confirmed as essential for ECR to CO. The structural reconstruction of LSA0.05M during ECR is investigated, and we find that Ag^+ in the near-surface of LSA0.05M evolves into small metallic Ag particles, enabling the in operando formation of an interface between the Ag and perovskite. Compared to a physical mixture of Ag and $La_{0.8}Sr_{0.2}MnO_{3-\delta}$ (LSM), the in operando-formed interface plays a significant role in improving ECR performance. A theoretical study indicates the in operando formation of an interface between the evolved Ag and the perovskite in LSA0.05M during ECR. The interface is shown to provide a favorable adsorption site for CO_2 and accelerate the desorption of the *CO intermediate to enhance ECR. Our work presents not only a novel efficient electrocatalyst for ECR but also a path for future work applying the in operando interface construction technique to advance electrochemical reactions.

2 | EXPERIMENTAL SECTION

2.1 | Materials synthesis

The perovskite oxides $LaMnO_3$, LSM, LSA0.03M, LSA0.05M, and LSA0.1M were synthesized by a combined ethylenediaminetetraacetic acid-citric acid (EDTA-CA) complexing sol–gel process. Briefly, taking the synthesis of LSA0.05M as an example, stoichiometric amounts of $La(NO_3)_3 \cdot 6H_2O$, $Sr(NO_3)_2$, $Ag(NO)_3$, and $Mn(CH_3COO)_2 \cdot 4H_2O$ (all of the analytical grade; Sinopharm Chemical Reagent Co., Ltd.) were dissolved in deionized water. Then CA and EDTA (Sinopharm Chemical Reagent Co., Ltd.) were added in sequence as complexing agents at a molar ratio of 2:1:1 for CA/EDTA/total metal ions. The pH value of the solution was adjusted to ~6 with the help of an aqueous ammonium hydroxide solution (28 wt.% NH_3 in H_2O; Sinopharm Chemical Reagent Co., Ltd.). The solution was intensively and continuously stirred at 90°C for 4 h to yield a transparent gel. This gel was first heated at 200°C for 8 h and then calcined in pure O_2 at 800°C for 5 h to obtain the final perovskite powder. Polycrystalline Ag foil (0.127 mm thick, 99.9%, annealed) was purchased from Alfa Aesar. Ag powder (99.9% metals basis, 1 μm) was purchased from Aladdin Industrial Corporation. All chemicals were used as received without further purification.

2.2 | Characterization

The crystal structure of the catalysts was studied by laboratory X-ray diffraction (Lab. XRD) patterns acquired on a Rigaku Smartlab with filtered Cu-Kα radiation, synchrotron X-ray diffraction (Syn. XRD) using synchrotron radiation at the TLS BL01C2 of NSRRC in Taiwan, China ($\lambda = 0.825847(56)$ Å), and high-resolution neutron powder diffraction (NPD) using the high-resolution neutron powder diffractometer Echidna[45] at the Australian Nuclear Science and Technology Organization ($\lambda = 2.43733(314)$ Å), respectively. The wavelengths of the NPD and Syn. XRD were determined using data for the $La^{11}B_6$ NIST (National Institute of Standards and Technology) standard reference material 660b. GSAS-II was employed to perform a combined Rietveld analysis of the Syn. XRD and NPD data using the starting phase with $R\bar{3}c$ space group symmetry.[46] High-resolution transmission electron microscopy (HRTEM), selected area electron diffraction (SAED), high-angle annular dark-field scanning transmission electron microscopy (HAADF-STEM), and energy-dispersive X-ray spectroscopy mapping were performed on a transmission electron microscope (FEI Tecnai G2T20) operating at 200kV. Scanning electron microscopy (SEM) images were obtained using a scanning electron micro-analyzer (Hitachi S-4800). X-ray photoelectron spectroscopy (XPS) data were obtained using a PHI5000 VersaProbe spectrometer with an Al-Kα X-ray source. N_2 adsorption–desorption was performed on a BELSOR-II instrument using the Brunauer–Emmett–Teller (BET) and Barrett–Joyner–Halenda methods to analyze the specific surface area and pore volume distribution of the samples.

Soft and hard XAS were conducted at the 11 A beamline of TPS and 44 A beamline of TLS in NSRRC (Taiwan, China), respectively. The soft XAS data were measured in total electron yield (TEY) mode and hard XAS data were recorded in transmission mode.

2.3 | Electrode preparation and ECR performance measurements

The as-prepared perovskite catalyst (10 mg) and carbon black (Super P Li, 10 mg; LiZhiYuan) were ultrasonically suspended in a mixture containing Nafion solution (5 wt%, 0.1 mL; DuPont) and absolute ethanol (1 mL, analytical reagent from Sinopharm Chemical Reagent Co., Ltd.) to form the electrode ink. Then, 30 μL of this homogeneous ink was transferred onto a prepolished glassy carbon electrode (GCE) with a diameter of 8 mm. The electrode was naturally dried at room temperature serving as the working electrode.

Electrochemical reduction performance was evaluated in a gas-tight H-cell reactor at 25°C. A Nafion 117 membrane was mounted in the middle of the cell for the separation of two chambers. The GCE and a reference electrode (Ag/AgCl) were fixed in the cathodic chamber,

while a Pt foil counter electrode was used in the anodic chamber. Each chamber was filled with 50 mL $KHCO_3$ (99.99%; Macklin) electrolyte (0.1 M), leaving a ~50 mL headspace. The applied potentials and the current were controlled by a CHI 760E workstation, and all potentials were recalculated into RHE by E (V vs. RHE) = E (V vs. Ag/AgCl) + 0.1989 + 0.0591 × pH unless otherwise stated. CO_2 with high purity (99.999%; Shangyuan) was purged into the H-cell for ~1 h before the reaction and was continuously supplied at a rate of 30 mL min^{-1} during the ECR measurement.

Gaseous products were directly imported into and analyzed by an online gas chromatograph (GC; HOPE 9860) with a thermal conductivity detector and flame ionization detectors. The liquid-phase products were detected by proton nuclear magnetic resonance (^{1}H NMR) spectroscopy using a Bruker ACF-400 instrument.

2.4 | Density functional theory (DFT) calculations

All calculations were performed using the Vienna Ab-initio Simulation Package.[47] To address the surface dipole moment in the periodic boundary condition, a dipole correction was included.[48] The projector-augmented wavefunction method describing electron-core interactions was employed.[49] The electron exchange-correlation was described through the Perdew–Burke–Ernzerhof functional in a plane wave pseudopotential implementation within the generalized gradient approximation.[50] Grimme's semi-empirical correction for the dispersion potential (DFT-D3) was applied to include long-range dispersion.[51] The plane wave cutoff energies were chosen to be 700 and 450 eV for the bulk conventional crystal cells and the slab models, respectively. A gamma-centered $3 \times 3 \times 1$ k-points grid in the Brillouin zone was automatically generated through the Monkhorst–Pack technique.[52] Gaussian smearing of width 0.1 eV was applied. The electronic self-consistent iteration convergence criterion was set to be 1.0×10^{-5} eV, and the convergence tolerance of force acting on each free atom was 0.03 eV/Å.

The bulk $LaMnO_3$ conventional crystal structure obtained from the Crystallography Open Database[53] (ID # 1006141,[54] a = 5.537 Å, b = 5.747 Å, c = 7.693 Å, $\alpha = \beta = \gamma = 90°$) was first fully relaxed. Then the (001) slabs were cleaved from the optimized bulk crystal cell. There are two types of truncated terminations of (001) crystal surface, that is, the LaO termination and the MnO_2 termination. The calculated cleavage energy of the surface with the LaO termination is smaller (Note S1); therefore, the LaO (001) surface model was used to

investigate the ECR mechanism in the present study. The (2 X 2) eight-layer-supercells were constructed with a 20-Å vacuum space along the z-axis to avoid the interaction between two adjacent images. The coordinates of the slabs were first optimized without adsorbates. The La^{3+} in the converged slab models was then substituted by six Sr^{2+} and two Ag$^+$ to mimic the LSA0.05M (001) surface. To study the effect of doped Ag$^+$ and Sr^{2+}, the model with two Ag$^+$ substituted two La^{3+} in the top LaO layer (referred to as LSA0.05M (001)-Ag model) and the model with two Sr^{2+} substituted two La^{3+} in the top LaO layer (referred to as LSA0.05M (001)-Sr model) were built. The doped surfaces proceeded to the optimization procedure (Figure S20). The CO and COOH intermediates with several different initial configurations were placed on the optimized $LaMnO_3$ and LSA0.05M (001) surfaces, and then the systems were optimized to obtain the binding configurations, during which the bottom four atomic layers were fixed. The adsorption energy was calculated using the following Equation 1:

$$\Delta E_{ads} = E_{slab+adsorbate} - E_{slab} - E_{adsorbate}, \quad (1)$$

where $E_{slab + adsorbate}$, E_{slab}, and $E_{adsorbate}$ are the energy of the surface with adsorbate, the energy of the surface without adsorbate, and the energy of the isolated adsorbate, respectively. A negative value of ΔE_{ads} means stable adsorption of the adsorbate on the perovskite surface, the more negative the more stable.

3 | RESULTS AND DISCUSSION

3.1 | Characterization of pristine perovskite oxide

We prepared LSM for comparison with LSA0.05M. Both catalysts were prepared by a sol–gel method.[55,56] Their crystal structures were first investigated by Lab. XRD with filtered Cu Kα radiation. As seen in Figure 1A, all diffraction peaks of LSM and LSA0.05M were indexed to a single-phase perovskite oxide, demonstrating phase purity[57,58] and the successful doping of Ag into the perovskite host lattice. Considering the small amount of Ag in LSA0.05M and to gain more information from the O and Mn in the presence of the heavier metals, Syn. XRD and NPD were employed, respectively, to further confirm the phase and structure of LSA0.05M. Combined structural refinement using both Syn. XRD and NPD data (refinement profiles are shown in Figure 1B,C and refined parameters are summarized in Table S1) confirmed $R\bar{3}c$ space group symmetry (Figure S1). HRTEM image of LSA0.05M exhibited a (102) interplanar
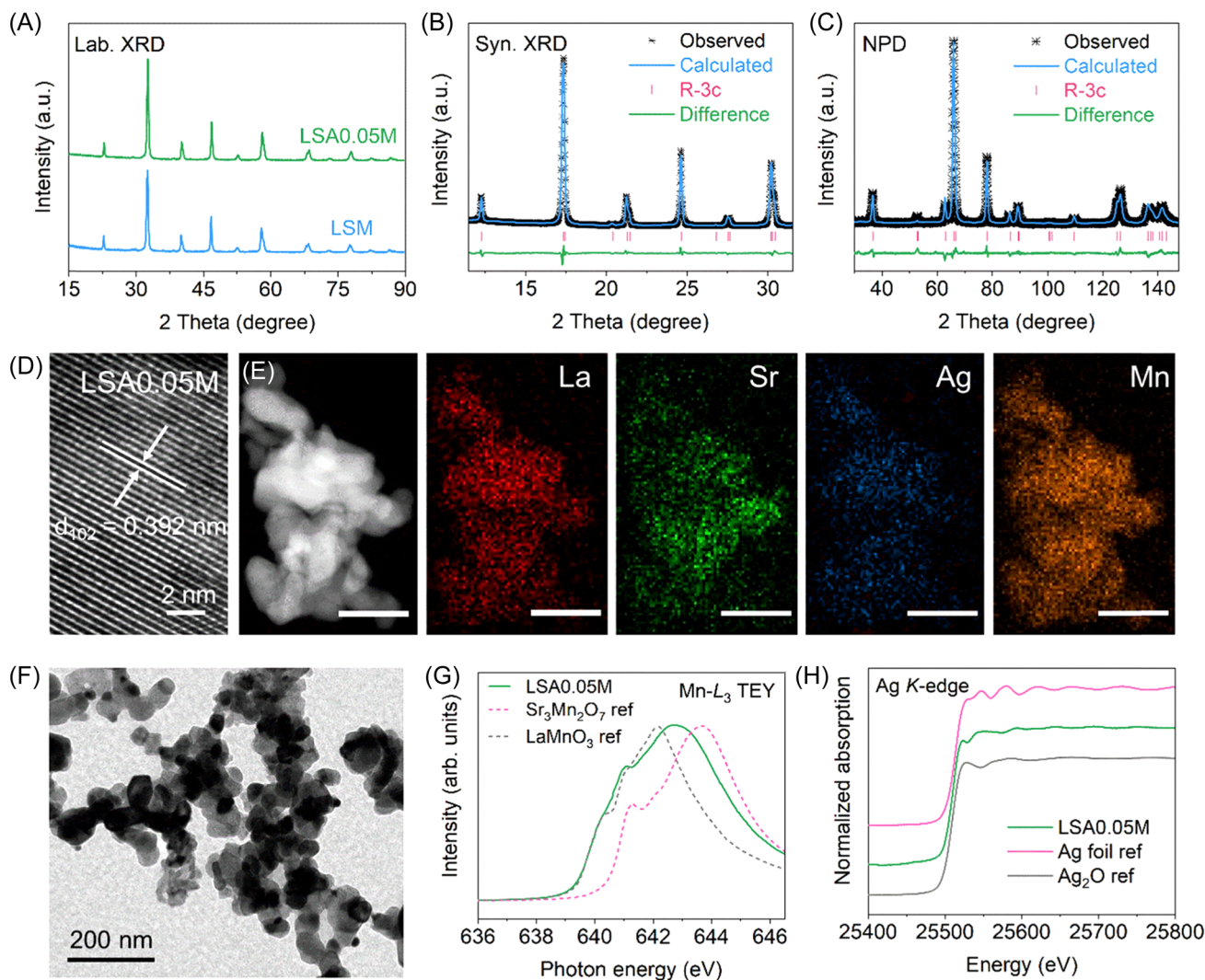
FIGURE 1 Structural characterization. (A) Lab. XRD data of LSM and LSA0.05M. Data are shown as a line and offset in y for clarity. Joint Rietveld refinement profiles using (B) Syn. XRD and (C) NPD data of LSA0.05M. (D) HRTEM image of LSA0.05M. (E) HAADF-STEM image of LSA0.05M and the corresponding elemental mapping. The scale bar is 100 nm. (F) TEM image of LSA0.05M. (G) Soft XAS data at the Mn-L_3 edge collected in TEY mode for LSA0.05M and two reference samples. (H) XANES spectra at the Ag K-edge for LSA0.05M, Ag_2O, and Ag foil samples. HAADF-STEM, high-angle annular dark-field scanning transmission electron microscopy; HRTEM, high-resolution transmission electron microscopy; Lab. XRD, laboratory X-ray diffraction; LSM, $La_{0.8}Sr_{0.2}MnO_{3-\delta}$; LSA0.05M, $(La_{0.8}Sr_{0.2})_{0.95}Ag_{0.05}MnO_{3-\delta}$; NPD, neutron powder diffraction; Syn. XRD, synchrotron-based X-ray diffraction; TEM, transmission electron microscopy; TEY, total electron yield; XANES, X-ray absorption near edge structure; XAS, X-ray absorption spectroscopy.

distance of 3.92 Å (Figure 1D). HAADF-STEM and corresponding elemental mapping of LSA0.05M (Figure 1E) demonstrated a homogeneous distribution of La, Sr, Ag, and Mn, further confirming the uniform doping of Ag into the perovskite oxide. The morphology of LSM and LSA0.05M (Figure S2 and Figure 1F) was studied using SEM and TEM. Different from typical sintered particles of (sub)micrometer-scale size,[59] both LSM and LSA0.05M samples displayed interconnected nanoparticles of 30–50 nm. This conclusion is supported by BET surface area and calculated pore volume distribution using nitrogen adsorption and desorption isotherms (Figure S3). We note that active site exposure

likely increases with the specific surface area along with decreasing sizes of particles and is generally beneficial to improving the performance of heterogeneous catalysis.

The electronic structures of the catalysts were first explored by surface-sensitive XPS.[60–62] Both La and Sr in LSM and LSA0.05M samples share similar chemical states (Figure S4A–C). The presence of Ag^+ in LSA0.05M was directly confirmed by the Ag 3d spectra (Figure S4E). The binding energy of Mn in perovskite oxides may be affected by both the doping of Ag and the oxygen vacancy concentration (Figure S4D,F).[33,58] Soft XAS at the Mn-L edge was performed in TEY mode, which is very sensitive to the valence state[63–65] and the local environment of Mn

ions.[66,67] As shown in Figure 1G, the Mn L_3 spectrum of LSA0.05M locates between those of Mn^{3+} reference $LaMnO_3$ and Mn^{4+} reference $Sr_3Mn_2O_7$, indicating the $Mn^{3.5+}$ valence state. The fitting result of soft XAS at Mn $L_{2,3}$ edge further confirmed the $Mn^{3.5+}$ valence state in LSA0.05M (Figure S5). The hard X-ray absorption near edge structure spectra at the Ag K-edge indicate the oxidation state of Ag^+ in the perovskite lattice of LSA0.05M by comparison with those of Ag_2O and Ag foil references (Figure 1H).

It is noted that the existence of Ag_2O in LSA0.05M is nearly impossible as Ag_2O will break down into metallic Ag at high temperatures (~300°C).[10] Our materials characterization experiments, therefore, support LSA0.05M being phase pure.

3.2 | Electrocatalytic performance measurements

Measurements of the electroreduction of CO_2 were conducted in 0.1 M $KHCO_3$ in a Nafion membrane-separated H-type cell. Step electrolysis experiments at various potentials were performed on the prepared catalysts to evaluate their selectivity and activity. The gaseous and liquid products were analyzed by an online GC and offline H^1 nuclear magnetic resonance (H^1 NMR)

spectroscopy, respectively. For the pure $LaMnO_3$ and LSM catalysts, only H_2 could be detected, indicating catalytic activity for HER rather than ECR (Figure S6).

The doping of small amounts of Ag into the perovskite lattice creates active sites and dramatically activates the ECR performance (Figure 2). The total current of LSA0.05M outperforms LSM, roughly indicating the effectiveness of Ag doping to enhance ECR activity (Figure S7). Then, the mass activity of LSA0.05M was obtained by normalizing the current to the mass of Ag in LSA0.05M. As seen in Figure 2A, the total current density reaches ~75 mA mg^{-1} at an applied potential of −0.9 V versus RHE. When the potential shifts to −1.2 V versus RHE, the current density reaches 400 mA mg^{-1}. The selectivity of LSA0.05M at various potentials is displayed in Figure 2B. The FE of CO presented a volcano-shaped relationship with the applied potentials, where the maximum of 84.3% was achieved at a moderate overpotential of 0.79 V. The FE of CO achieved by LSA0.05M is much higher than that of traditional polycrystalline Ag foil.[10] A small amount of CH_4 (FE = 2.8%) was detected at a high overpotential of 1.09 V. Generally speaking, CH_4 product is more often observed in Cu-based catalysts. However, CH_4 can also be produced by metal Ag catalyst from ECR reaction.[68] From the point of Kuhl et al.,[68] the activity and selectivity for ECR to methane are related to the surface's binding
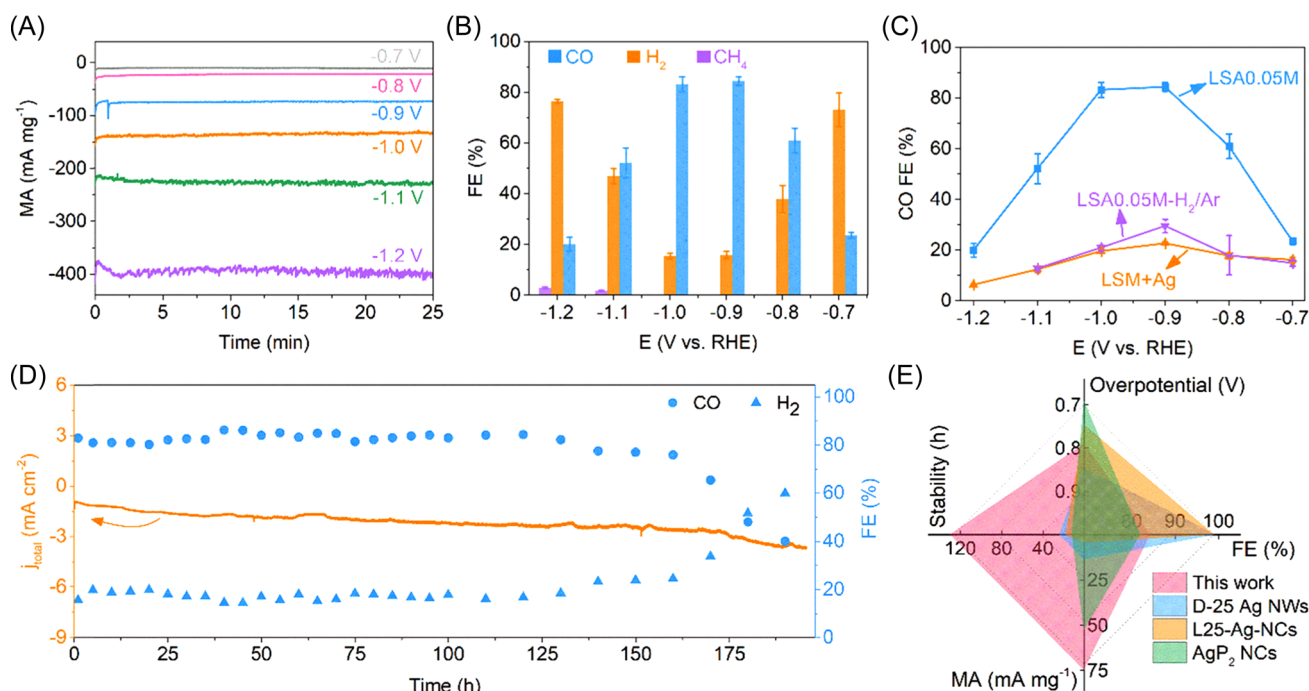

FIGURE 2 Electrochemical reduction in 0.1 M $KHCO_3$ solution. (A) Mass activity (MA) of LSA0.05M at different potentials. (B) FE of LSA0.05M at different potentials. (C) CO FE of LSA0.05M, LSA0.05M-H_2/Ar, and LSM + Ag catalysts at different potentials. Lines through the points are a guide to the eye. (D) Current density j_{total}, CO FE, and H_2 FE of LSA0.05M at −0.9 V. (E) Performance parameter comparison including stability (j_{total}), MA, and CO FE, against overpotential, for several representative Ag-based catalysts. FE, Faradaic efficiency; LSM, $La_{0.8}Sr_{0.2}MnO_{3-\delta}$; LSA0.05M, $(La_{0.8}Sr_{0.2})_{0.95}Ag_{0.05}MnO_{3-\delta}$.

energy of CO. Typically, CO intermediate adsorbs weakly on the Ag surface, making CO reduction competing against the very kinetically fast process of CO desorption. Therefore, only at the extremely high overpotential can the rate of CO reduction to CH_4 begin to compete with the rate of CO desorption. In addition, the oxophilicity of the surface also plays a significant role in determining the CH_4 selectivity. The perovskite surface within the perovskite–Ag interface may improve the binding energy of O_{ads}, thus promoting the production of CH_4 at a high overpotential.

Furthermore, considering the possible evolution of Ag from the perovskite lattice during ECR as reported for another perovskite catalyst,[38] two further samples were prepared for comparison: LSA0.05M treated under a reducing atmosphere at high temperature (LSA0.05M-H_2/Ar) and a sample produced by the physical mixing of LSM with Ag (LSM + Ag). XRD peaks corresponding to the Ag phase are weak in LSA0.05M-H_2/Ar (Figure S8A), possibly owing to the tiny amount of Ag; however, SEM shows evidence for an evolved phase in LSA0.05M/H_2-Ar (Figure S8B). The mass concentration of Ag in LSM + Ag is a little higher than that in LSA0.05M. The XRD data confirm the expected phase composition of the metallic Ag and LSM in LSM + Ag (Figure S8A). As shown in Figure 2C and S8C, both catalysts showed a remarkably inferior ability to convert CO_2 into CO, with limited FE (<30%) at all tested potentials. This result possibly indicates the crucial role of the interface formed between the metal and perovskite in enhancing ECR. The determination of the structure and composition of LSA0.05M after ECR is important to understanding this further.

The stability of LSA0.05M is impressive (Figure 2D), with a nearly unchanged CO FE (~82.2%) and geometric current density after 130 h of electrolysis. A comprehensive assessment of the ECR performance of various Ag-based catalysts will compare the multiple key parameters jointly. Accordingly, the mass activity, CO FE, and stability of current density alongside the corresponding overpotential, for some representative Ag-based catalysts including LSA0.05M in $KHCO_3$ electrolyte are, summarized in Table S2 and presented as a four-parameter radar map for selected catalysts in Figure 2E.[69–71] This comparison reveals that despite a mild-range overpotential and CO FE, the mass activity and current density stability of LSA0.05M are remarkably superior to other catalysts.

The effect of the Ag concentration doped into the perovskite on ECR performance is also discussed. Two other catalysts, $(La_{0.8}Sr_{0.2})_{0.97}Ag_{0.03}MnO_3$ (LSA0.03M) and $(La_{0.8}Sr_{0.2})_{0.9}Ag_{0.1}MnO_3$ (LSA0.1M), were prepared using a similar method to LSA0.05M. Figure S9A,B shows Lab.

XRD and Syn. XRD data for these samples revealing the appearance of peaks corresponding to metallic Ag in LSA0.1M. The morphologies of LSA0.03M and LSA0.1M are similar to that of LSA0.05M, as shown in Figure S9C,D. The ECR performance of these catalysts was then tested by comparing the CO FE and total current density as a function of potential for the samples as a function of Ag concentration, as shown in Figure S10, with the LSA0.05M catalyst displaying the best CO FE among these. This result may inspire future work to optimize the concentration of Ag in this perovskite for promoting ECR performance.

3.3 | In operando formation of the interface between metallic Ag and perovskite phases

Typically, perovskite oxide catalysts may suffer structure and/or phase reconstruction, particularly the partial evolution of metallic elements due to the applied cathodic potential.[38] This behavior may offer a great opportunity to in operando create an interface between the evolved metal and the bulk perovskite phase, enabling active sites in the interface region with unique catalytic properties. Figure 3A shows a schematic representation of the interface between the evolved Ag and perovskite phases. The morphology of the LSA0.05M catalyst seems to be unchanged after ECR at different times, as shown in Figure S11. Syn. XRD data of LSA0.05M following 2 h of catalytic reaction (LSA0.05M-after ECR) is shown in Figure 3B, together with data for several reference samples, where reflections from metallic Ag in the data for LSA0.1M are identified by asterisks. Data reveal that the bulk crystal structure of LSA0.05M is preserved after ECR, as corroborated by Lab XRD (Figure S12A). Similarly, the crystal structure of LSA0.05M-after ECR is further confirmed using an HRTEM image, as shown in Figure S12B. Given the relatively minor amount of Ag in LSA0.05M, the possibility of Ag evolution from the perovskite cannot be arbitrarily excluded.

As shown in Figure 3C, the Mn L_3 XAS spectrum of LSA0.05M after ECR exhibits a strong sharp peak at 640.2 eV, which locates at the same energy as the main peak of the MnO spectrum, demonstrating a decrease in the valence state of Mn ions after ECR, which may protect the bulk perovskite structure from the reductive electrolysis conditions. The change of the Ag valence state in LSA0.05M was then investigated. Considering that evolved Ag may adhere to the perovskite surface, we utilized XPS (a surface-sensitive technique) to determine the Ag valence state. XPS in Ag 3d region of LSA0.05M
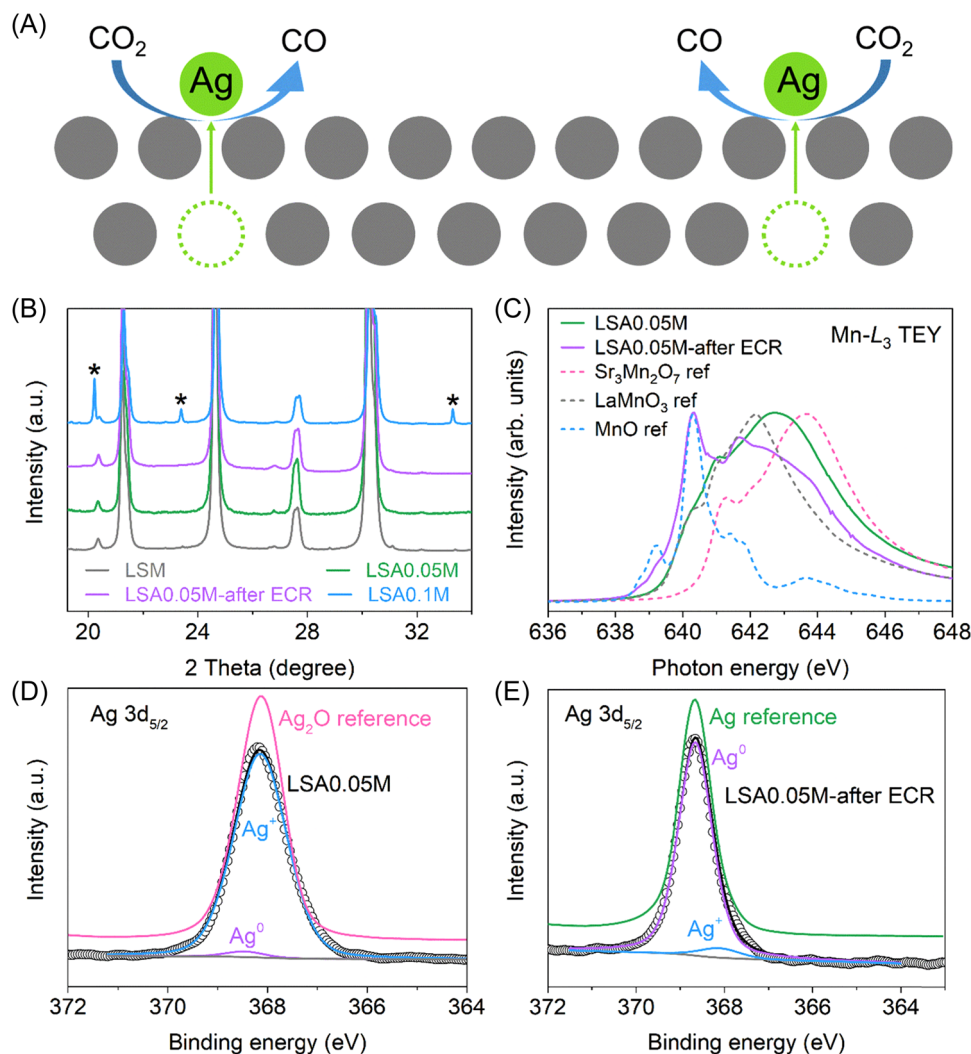
FIGURE 3 (A) Schematic representation of the interface between the evolved Ag and perovskite, where the dashed green circle represents a vacancy formed. (B) Syn. XRD data of catalysts. Data are shown as a line and offset in y for clarity. (C) Ex situ XAS at the Mn *L*-edge. XPS data and analysis at the Ag $3d_{5/2}$ region of (D) LSA0.05M and (E) LSA0.05M-after ECR of 2 h. ECR, electrochemical CO_2 reduction; LSA0.05M, $(La_{0.8}Sr_{0.2})_{0.95}Ag_{0.05}MnO_{3-\delta}$; Syn. XRD, synchrotron-based X-ray diffraction; XAS, X-ray absorption spectroscopy; XPS, X-ray photoelectron spectroscopy.

and LSA0.05M-after ECR alongside their analysis are shown in Figure 3D,E and Figure S12C. The binding energy of Ag $3d_{5/2}$ of the pristine LSA0.05M was similar to that of the Ag_2O reference. Analysis of the XPS data revealed a concentration of 98% Ag^+ in LSA0.05M, indicating the successful doping of Ag into the perovskite lattice. After ECR, the binding energy of Ag $3d_{5/2}$ is shifted positively, suggesting the decrease of Ag valence state in the LSA0.05M-after ECR sample. A concentration of 95% for Ag^0 is determined from the XPS data at the Ag $3d_{5/2}$ region. Furthermore, the SAED of the LSA0.05M-after ECR sample (Figure S12D,E) reveals perovskite lattice (102(_)) and (104) planes, as well as the much weaker metal Ag lattice (111) plane, confirming the coexistence of these two phases. The change of

crystal and electronic structure of catalysts following ECR evidences the evolution of Ag from the perovskite lattice during ECR. The in operando-evolved Ag presents a great dispersity with a small particle size on the surface, creating an interface between Ag and the bulk perovskite that correlates with enhanced ECR performance. As revealed in the theoretical calculations, this interface may provide important adsorption sites for CO_2, weakening the adsorption of *COOH and *CO to facilitate CO production.
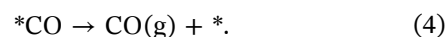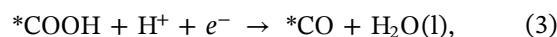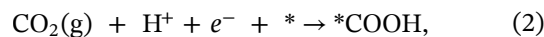
The evolution process of Ag from the perovskite may also be revealed by electrochemical working data. Figure S13 shows current during applied cathodic potential, which decreased initially (within ~300 s) before reaching a steady stage. This phenomenon is similar to

previous research reporting the in operando transition of Ag_2O to Ag during ECR.[10] XPS result of the material after 300 s electrolysis confirmed a decrease of the Ag valence state, supporting the evolution of Ag from the perovskite lattice, as shown in Figure S14. The linear sweep voltammetry curves and electrochemical impedance spectroscopy after ECR at different times were collected to further elucidate the reconstruction process, as shown in Figure S15. The current density and charge transfer process of LSA0.05M were improved after 15 min ECR reaction, which was possibly due to the evolution of Ag and the formation of the perovskite–Ag interface. In summary, we propose that the initial decrease in current density corresponds to the evolution of Ag from the perovskite lattice, after which the electrochemical CO_2 reduction reaction proceeds at the formed Ag–perovskite interface.

3.4 | Theoretical studies

We performed a theoretical study based on DFT calculations to investigate the electrochemical behavior of LSA0.05M during ECR. For comparison, the model based on $LaMnO_3$ perovskite oxide was also constructed to obtain insight into the effects of Sr^{2+} and Ag^+ doping on ECR performance. We studied the thermodynamic properties of reactions and the adsorption properties of intermediates important to ECR on the (001) crystal surfaces using the DFT method. According to previous studies,[10,26,72] the following reaction mechanism is considered:

$$CO_2(g) + H^+ + e^- + * \rightarrow {}^*COOH, \quad (2)$$

$$^*COOH + H^+ + e^- \rightarrow {}^*CO + H_2O(l), \quad (3)$$

$$^*CO \rightarrow CO(g) + *. \quad (4)$$

The most stable adsorption configurations of carboxyl (*COOH) and *CO species (* denotes one adsorption site) on $LaMnO_3$ (001) surface, LSA0.05M (001)-Ag surface, and LSA0.05M (001)-Sr surface, respectively, are shown in Figure 4. The ΔE_{ads} of *COOH and *CO on the $LaMnO_3$ (001) surface are −4.38 and −1.71 eV, respectively (Figure 4A,D). Both *COOH and *CO adsorb at the bridge site of two La^{3+}. The C atom of *COOH/*CO is above the second-layer O atom (Figure S16). The ΔE_{ads} of *COOH and *CO on the LSA0.05M (001)-Sr surface is −4.53 and −0.34 eV, respectively. That is, the Sr site results in stronger adsorption of *COOH and weaker adsorption of *CO compared with the undoped $LaMnO_3$ (001) surface. Both *COOH and *CO adsorb over the Sr^{2+} (Figure 4C,F).

Relatively, the ΔE_{ads} of *COOH and *CO on the LSA0.05M (001)-Ag surface are −3.71 and −1.47 eV, respectively, which are less negative with respect to those

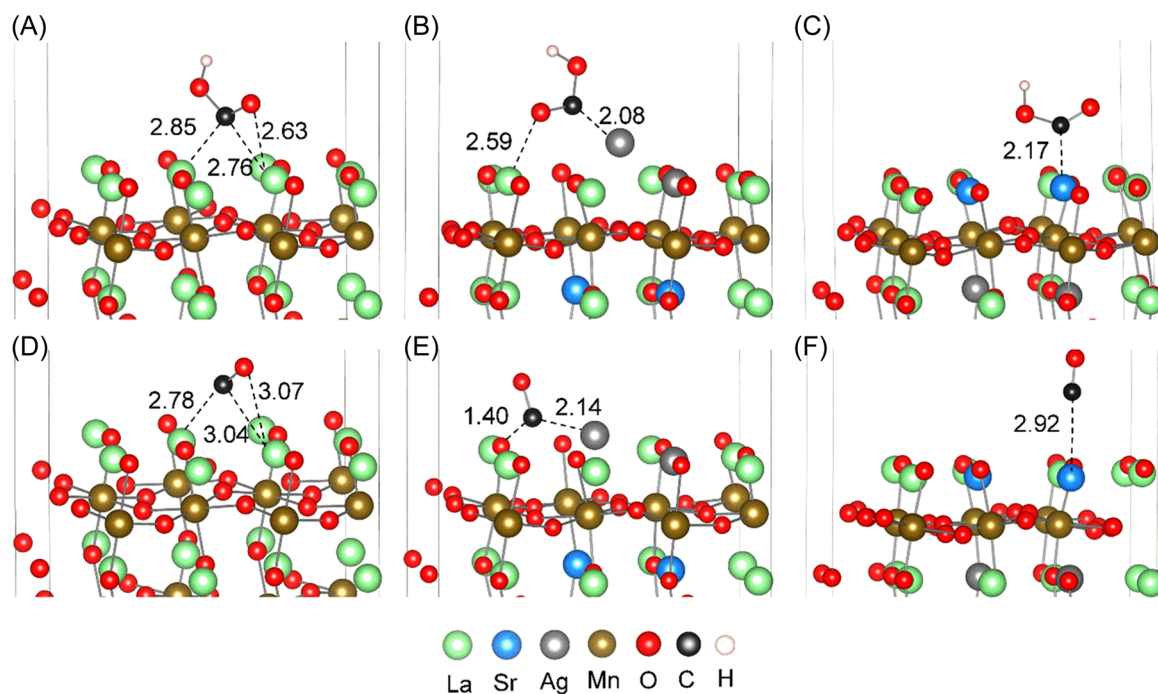**FIGURE 4** The most stable adsorption configurations of *COOH on (A) $LaMnO_3$ (001) surface, (B) LSA0.05M (001)-Ag surface, and (C) LSA0.05M (001)-Sr surface. The most stable adsorption configurations of *CO on (D) $LaMnO_3$ (001) surface, (E) LSA0.05M (001)-Ag surface, and (F) LSA0.05M (001)-Sr surface. These distances are all in Angstroms. LSA0.05M, $(La_{0.8}Sr_{0.2})_{0.95}Ag_{0.05}MnO_{3-\delta}$.

on LaMnO$_3$ (001) surface. The possible reason might be that the adsorption of COOH and CO leads to the evolution of nearby Ag$^+$ from the crystal lattice to form Ag (Figure 4B,E). This is consistent with the current experimental results. The weak binding of Ag to ECR intermediates has been widely reported.[28] We also calculated the adsorption of COOH and CO on the three low-index crystal surfaces of Ag (Ag (100), Ag (110), and Ag (111)). The ΔE_{ads} of *COOH and *CO on the three surfaces are ca. −2.0 and −0.5 eV (Table S3), respectively, demonstrating much weaker adsorption compared with the perovskite.

To get a better understanding of the adsorption properties of COOH and CO at the interface formed by LaMnO$_3$ and Ag, we constructed the LaMnO$_3$–Ag cluster interface model as shown in Figure S17. The ΔE_{ads} of *COOH and *CO (Figure S18) at the interface are −3.74 and −1.42 eV, respectively, which are comparable with those on the LSA0.05M (001)-Ag surface.

Briefly, our calculations indicate the formation of an interface between the perovskite and the evolved Ag in LSA0.05M during ECR. This interface may serve as an important adsorption site for ECR to CO, weakening the adsorption of *COOH and *CO.

The calculated free energy diagrams at 0 V versus the reversible hydrogen electrode (RHE) and pH 6.8 are shown in Figure 5. The reaction (2) is uphill on both LaMnO$_3$ (001) and LSA0.05M (001)-Ag surfaces with a reaction free energy (ΔG_r) of 1.04 and 0.64 eV, respectively, revealing that the protonated dissociation of *COOH to *CO is the potential determining step (PDS). The limiting potential (U_L) on the LSA0.05M (001)-Ag surface (−0.64 V) is 0.4 V higher than that on the LaMnO$_3$ (001) surface (−1.04 V). This means that the doped Ag adsorption site reduces the overpotential of ECR to CO dramatically. The free energy diagram of the LSA0.05M (001)-Sr surface is different from those of the LaMnO$_3$ (001) and the LSA0.05M (001)-Ag surfaces in which the reaction (2) is the potential determining step resulting in a U_L of −1.21 V. This indicates that the doped Sr adsorption site increases the overpotential of ECR to CO.

The ΔG_r of reaction (2) is −0.84 and −0.10 eV on the LaMnO$_3$ (001) and LSA0.05M (001)-Ag surfaces, respectively, demonstrating that the activation of CO$_2$ via protonation to form *COOH is facilitated on both surfaces. The ΔG_r of reaction (4) is 0.82 and 0.50 eV on the LaMnO$_3$ (001) and LSA0.05M (001)-Ag surfaces, respectively, indicating that the desorption of *CO is nonspontaneous on both surfaces. The free energy diagram property of the LaMnO$_3$–Ag cluster interface model (Figure S18C) is quite similar to that of the LSA0.05M (001)-Ag surface.
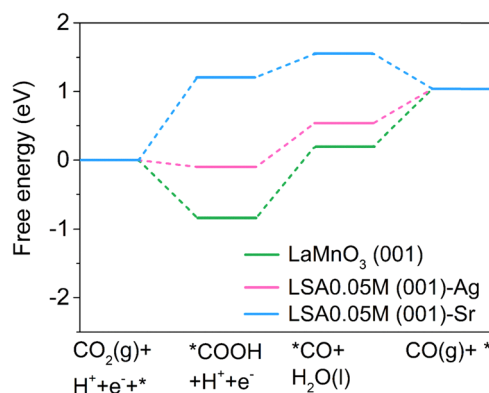

FIGURE 5 The calculated free energy for ECR to CO on LaMnO$_3$ (001), LSA0.05M (001)-Ag surface, and LSA0.05M (001)-Sr surface. LSA0.05M, $(La_{0.8}Sr_{0.2})_{0.95}Ag_{0.05}MnO_{3-\delta}$.

Nevertheless, our calculations reveal that the doped Ag adsorption site, which shows the potential to form the perovskite–Ag interface, weakens the binding of CO and COOH, reducing the overpotential. Therefore, an appropriate doping concentration should benefit the production of CO.

The free energy diagrams of the LaMnO$_3$ (001) and the LSA0.05M (001)-Ag surfaces are quite different from the case of Ag surfaces in which the formation of *COOH is the PDS, while the dissociation of *COOH and the desorption of *CO are downhill due to the weak adsorption of *COOH and *CO as shown in Figure S19. Similar thermodynamics of Ag for ECR has been reported previously.[73,74] In conclusion, the calculations demonstrate that the LaMnO$_3$ perovskite can strongly adsorb *COOH and *CO, which facilitates activation of CO$_2$, and however, makes subsequent *COOH decomposition and *CO desorption harder. The Ag adsorption site of the doped LSA0.05M weakens the adsorption of *COOH and *CO due to the formation of Ag from lattice Ag$^+$. This partially explains the enhanced ECR performance on the in operando-formed perovskite–Ag interface.

4 | CONCLUSION

We demonstrate the perovskite oxide LSA0.05M to be an efficient electrocatalyst for ECR to CO. Driven by a moderate overpotential (0.79 V), LSA0.05M exhibits a high CO FE of 84.3%, a remarkable mass activity of 75 A g^{-1}, and stability of 130 h. By comparing with the inactive counterpart of LSM, the doping of Ag into the perovskite is confirmed to be necessary for high-performance ECR. The concentration of Ag is an influential factor and can be optimized for better catalytic performance. Comparison of the crystal and electronic

structure of LSA0.05M before and after ECR evidences the in operando formation of an interface between the evolved Ag and the perovskite, where Ag presents as a uniform distribution with small particle size, benefiting ECR performance. Theoretical calculations also indicate the electrochemical reconstruction of LSA0.05M to form the experimentally observed Ag–perovskite interface and uncover a mechanism for enhanced catalysis involving weakened *COOH and *CO adsorption that enhances CO production. This study not only presents an excellent perovskite catalyst for ECR to CO but may inspire a new direction for the investigation of new electrocatalysts, especially perovskite oxides, for promoting electrochemical reactions.

CONFLICTS OF INTEREST
The authors declare no conflicts of interest.

ORCID
Wei Zhou 🔘 http://orcid.org/0000-0003-0322-095X
Zongping Shao 🔘 http://orcid.org/0000-0002-4538-4218

REFERENCES
1. Singh AK, Montoya JH, Gregoire JM, Persson KA. Robust and synthesizable photocatalysts for CO_2 reduction: a data-driven materials discovery. *Nat Commun*. 2019;10:443.
2. Sullivan I, Goryachev A, Digdaya IA, et al. Coupling electrochemical CO_2 conversion with CO_2 capture. *Nat Catal*. 2021;4(11):952-958.
3. Liang S, Jiang Q, Wang Q, Liu Y. Revealing the real role of nickel decorated nitrogen-doped carbon catalysts for electrochemical reduction of CO_2 to CO. *Adv Energy Mater*. 2021;11(36):2101477.
4. Cai Z, Wu Y, Wu Z, et al. Unlocking bifunctional electrocatalytic activity for CO_2 reduction reaction by win-win metal–oxide cooperation. *ACS Energy Lett*. 2018;3(11):2816-2822.
5. Ye W, Guo X, Ma T. A review on electrochemical synthesized copper-based catalysts for electrochemical reduction of CO_2 to C_{2+} products. *Chem Eng J*. 2021;414:128825.
6. Zhong M, Tran K, Min Y, et al. Accelerated discovery of CO_2 electrocatalysts using active machine learning. *Nature*. 2020;581(7807):178-183.
7. Xu C, Zhi X, Vasileff A, et al. Highly selective two-electron electrocatalytic CO_2 reduction on single-atom Cu catalysts. *Small Struct*. 2021;2(1):2000058.
8. Zhu DD, Liu JL, Qiao SZ. Recent advances in inorganic heterogeneous electrocatalysts for reduction of carbon dioxide. *Adv Mater*. 2016;28(18):3423-3452.
9. Kibria MG, Edwards JP, Gabardo CM, et al. Electrochemical CO_2 reduction into chemical feedstocks: from mechanistic electrocatalysis models to system design. *Adv Mater*. 2019;31(31):1807166.
10. Wu X, Guo Y, Sun Z, et al. Fast operando spectroscopy tracking in situ generation of rich defects in silver nanocrystals for highly selective electrochemical CO_2 reduction. *Nat Commun*. 2021;12:660.
11. Sun D, Xu X, Qin Y, Jiang SP, Shao Z. Rational design of Ag-based catalysts for the electrochemical CO_2 reduction to CO: a review. *ChemSusChem*. 2020;13(1):39-58.
12. Zou Y, Wang S. An investigation of active sites for electrochemical CO_2 reduction reactions: from in situ characterization to rational design. *Adv Sci*. 2021;8(9):2003579.
13. Huo H, Wang J, Fan Q, Hu Y, Yang J. Cu-MOFs derived porous Cu nanoribbons with strengthened electric filed for selective CO_2 electroreduction to C_{2+} fuels. *Adv Energy Mater*. 2021;11(42):2102447.
14. Chen J, Zhang H, Yu J, et al. Self-catalyzed formation of strongly interconnected multiphase molybdenum-based composites for efficient hydrogen evolution. *Carbon Energy*. 2022;4(1):77-87.
15. Gao D, Arán-Ais RM, Jeon HS, Roldan Cuenya B. Rational catalyst and electrolyte design for CO_2 electroreduction towards multicarbon products. *Nat Catal*. 2019;2(3):198-210.
16. Vasileff A, Xu C, Jiao Y, Zheng Y, Qiao S-Z. Surface and interface engineering in copper-based bimetallic materials for selective CO_2 electroreduction. *Chem*. 2018;4(8):1-23.
17. Yang C-H, Nosheen F, Zhang Z-C. Recent progress in structural modulation of metal nanomaterials for electrocatalytic CO_2 reduction. *Rare Metals*. 2021;40(6):1412-1430.
18. Shah SSA, Najam T, Wen M, Zang SQ, Waseem A, Jiang HL. Metal-organic framework-based electrocatalysts for CO_2 reduction. *Small Struct*. 2022;3(5):2100090.
19. Liu Y-J, Shao P, Gao M-Y, Fang W-H, Zhang J. Synthesis of Ag-doped polyoxotitanium nanoclusters for efficient electrocatalytic CO_2 reduction. *Inorg Chem*. 2020;59(16):11442-11448.
20. Sun Z, Wu X, Guan D, et al. One pot-synthesized Ag/Ag-doped CeO_2 nanocomposite with rich and stable 3D interfaces and Ce^{3+} for efficient carbon dioxide electroreduction. *ACS Appl Mater Interfaces*. 2021;13(50):59993-60001.
21. Wang Y, Han P, Lv X, Zhang L, Zheng G. Defect and interface engineering for aqueous electrocatalytic CO_2 reduction. *Joule*. 2018;2(12):2551-2582.
22. Meng X, Deng X, Zhou L, et al. A highly ordered hydrophilic-hydrophobic Janus bi-functional layer with ultralow Pt loading and fast gas/water transport for fuel cells. *Energy Environ Mater*. 2021;4(1):126-133.
23. Wang S, Kou T, Varley JB, et al. Cu_2O/CuS nanocomposites show excellent selectivity and stability for formate generation via electrochemical reduction of carbon dioxide. *ACS Mater Lett*. 2021;3(1):100-109.
24. Jia S, Zhu Q, Chu M, et al. Hierarchical metal-polymer hybrids for enhanced CO_2 electroreduction. *Angew Chem Int Ed*. 2021;60(19):10977-10982.

25. Rogers C, Perkins WS, Veber G, Williams TE, Cloke RR, Fischer FR. Synergistic enhancement of electrocatalytic CO_2 reduction with gold nanoparticles embedded in functional graphene nanoribbon composite electrodes. *J Am Chem Soc.* 2017;139(11):4052-4061.

26. Gao D, Zhang Y, Zhou Z, et al. Enhancing CO_2 electroreduction with the metal-oxide interface. *J Am Chem Soc.* 2017;139(16):5652-5655.

27. Lee CW, Shin S-J, Jung H, et al. Metal-oxide interfaces for selective electrochemical C-C coupling reactions. *ACS Energy Lett.* 2019;4(9):2241-2248.

28. Zong X, Zhang J, Zhang J, Luo W, Züttel A, Xiong Y. Synergistic Cu/CeO_2 carbon nanofiber catalysts for efficient CO_2 electroreduction. *Electrochem Commun.* 2020;114:106716.

29. Larrazábal GO, Martín AJ, Mitchell S, Hauert R, Pérez-Ramírez J. Synergistic effects in silver-indium electrocatalysts for carbon dioxide reduction. *J Catal.* 2016;343:266-277.

30. Ma S, Lan Y, Perez GM, Moniri S, Kenis PJ. Silver supported on titania as an active catalyst for electrochemical carbon dioxide reduction. *ChemSusChem.* 2014;7(3):866-874.

31. Zeng S, Kar P, Thakur UK, Shankar K. A review on photocatalytic CO_2 reduction using perovskite oxide nanomaterials. *Nanotechnology.* 2018;29(5):052001.

32. Yin W-J, Weng B, Ge J, Sun Q, Li Z, Yan Y. Oxide perovskites, double perovskites and derivatives for electrocatalysis, photocatalysis, and photovoltaics. *Energy Environ Sci.* 2019;12(2):442-462.

33. Amano M, Betancourt I, Sánchez Llamazares J, Huerta L, Sánchez-Valdés C. Mixed-valence $La_{0.80}(Ag_{1-x}Sr_x)_{0.20}MnO_3$ manganites with magnetocaloric effect. *J Mater Sci.* 2014;49(2):633-641.

34. Wang X, Dai J, Zhou C, et al. Engineering charge redistribution within perovskite oxides for synergistically enhanced overall water splitting. *ACS Mater Lett.* 2021;3(8):1258-1265.

35. Guan D, Zhou J, Hu Z, et al. Searching general sufficient-and-necessary conditions for ultrafast hydrogen-evolving electrocatalysis. *Adv Funct Mater.* 2019;29(20):1900704.

36. Zhu Y, Tahini HA, Hu Z, et al. Boosting oxygen evolution reaction by creating both metal ion and lattice-oxygen active sites in a complex oxide. *Adv Mater.* 2020;32(1):1905025.

37. Chen G, Hu Z, Zhu Y, et al. A universal strategy to design superior water-splitting electrocatalysts based on fast in situ reconstruction of amorphous nanofilm precursors. *Adv Mater.* 2018;30(43):1804333.

38. Chen S, Su Y, Deng P, et al. Highly selective carbon dioxide electroreduction on structure-evolved copper perovskite oxide toward methane production. *ACS Catal.* 2020;10(8):4640-4646.

39. Schwartz M, Cook RL, Kehoe VM, MacDuff RC, Patel J, Sammells AF. Carbon dioxide reduction to alcohols using perovskite-type electrocatalysts. *J Electrochem Soc.* 1993;140(3):614-618.

40. Pi Y, Guo J, Shao Q, Huang X. All-inorganic $SrSnO_3$ perovskite nanowires for efficient CO_2 electroreduction. *Nano Energy.* 2019;62:861-868.

41. Wang J, Cheng C, Huang B, et al. Grain-boundary-engineered La_2CuO_4 perovskite nanobamboos for efficient CO_2 reduction reaction. *Nano Lett.* 2021;21(2):980-987.

42. Singh RP, Arora P, Nellaiappan S, et al. Electrochemical insights into layered La_2CuO_4 perovskite: active ionic copper for selective CO_2 electroreduction at low overpotential. *Electrochim Acta.* 2019;326:134952.

43. Zhu J, Wang Y, Zhi A, et al. Cation-deficiency-dependent CO_2 electroreduction over copper-based Ruddlesden-Popper perovskite oxides. *Angew Chem Int Ed.* 2022;61(3):e202111670.

44. Sui R, Pei J, Fang J, et al. Engineering $Ag-N_x$ single-atom sites on porous concave N-doped carbon for boosting CO_2 electroreduction. *ACS Appl Mater Interfaces.* 2021;13(15):17736-17744.

45. Liss K-D, Hunter B, Hagen M, Noakes T, Kennedy S. Echidna-the new high-resolution powder diffractometer being built at OPAL. *Physica B Condens Matter.* 2006;385-386:1010-1012.

46. Toby BH, Von Dreele RB. GSAS-II: the genesis of a modern open-source all purpose crystallography software package. *J Appl Crystallogr.* 2013;46(2):544-549.

47. Kresse G, Furthmüller J. Efficient iterative schemes for ab initio total-energy calculations using a plane-wave basis set. *Phys Rev B.* 1996;54(16):11169-11186.

48. Bengtsson L. Dipole correction for surface supercell calculations. *Phys Rev B.* 1999;59(19):12301-12304.

49. Kresse G, Joubert D. From ultrasoft pseudopotentials to the projector augmented-wave method. *Phys Rev B.* 1999;59(3):1758-1775.

50. Perdew JP, Burke K, Ernzerhof M. Generalized gradient approximation made simple. *Phys Rev Lett.* 1996;77(18):3865-3868.

51. Grimme S, Ehrlich S, Goerigk L. Effect of the damping function in dispersion corrected density functional theory. *J Comput Chem.* 2011;32(7):1456-1465.

52. Monkhorst HJ, Pack JD. Special points for Brillouin-zone integrations. *Phys Rev B.* 1976;13(12):5188-5192.

53. Vaitkus A, Merkys A, Gražulis S. Validation of the crystallography open database using the crystallographic information framework. *J Appl Crystallogr.* 2021;54(2):661-672.

54. Rodríguez-Carvajal J, Hennion M, Moussa F, Moudden AH, Pinsard L, Revcolevschi A. Neutron-diffraction study of the Jahn-Teller transition in stoichiometric $LaMnO_3$. *Phys Rev B.* 1998;57(6):R3189-R3192.

55. Wu X, Yu J, Yang G, Liu H, Zhou W, Shao Z. Perovskite oxide/carbon nanotube hybrid bifunctional electrocatalysts for overall water splitting. *Electrochim Acta.* 2018;286:47-54.

56. Sun H, Xu X, Chen G, et al. Smart control of composition for double perovskite electrocatalysts toward enhanced oxygen evolution reaction. *ChemSusChem.* 2019;12(23):5111-5116.

57. Miao J, Duan X, Li J, et al. Boosting performance of lanthanide magnetism perovskite for advanced oxidation through lattice doping with catalytically inert element. *Chem Eng J.* 2019;355:721-730.

58. Zhou W, Shao Z, Liang F, et al. A new cathode for solid oxide fuel cells capable of in situ electrochemical regeneration. *J Mater Chem.* 2011;21(39):15343-15351.

59. Xu X, Chen Y, Zhou W, Zhong Y, Guan D, Shao Z. Earth-abundant silicon for facilitating water oxidation over iron-based perovskite electrocatalyst. *Adv Mater Interfaces.* 2018;5(11):1701693.

60. Tjeng L-H, Meinders MB, Van Elp J, Ghijsen J, Sawatzky GA, Johnson RL. Electronic structure of Ag_2O. *Phys Rev B.* 1990;41(5):3190-3199.

61. Altieri S, Tjeng L, Sawatzky G. Electronic structure and chemical reactivity of oxide-metal interfaces: MgO (100)/Ag (100). *Phys Rev B*. 2000;61(24):16948-16955.

62. Tjeng L, Meinders M, Sawatzky G. Electronic structure of clean and oxygen covered silver (110) surface. *Surf Sci*. 1990;236(3):341-368.

63. Burnus T, Hu Z, Hsieh HH, et al. Local electronic structure and magnetic properties of $LaMn_{0.5}Co_{0.5}O_3$ studied by x-ray absorption and magnetic circular dichroism spectroscopy. *Phys Rev B*. 2008;77(12):125124.

64. Nemrava S, Vinnik DA, Hu Z, et al. Three oxidation states of manganese in the barium hexaferrite $BaFe_{12-x}Mn_xO_{19}$. *Inorg Chem*. 2017;56(7):3861-3866.

65. Vasiliev AN, Volkova OS, Lobanovskii LS, et al. Valence states and metamagnetic phase transition in partially *B*-site-disordered perovskite $EuMn_{0.5}Co_{0.5}O_3$. *Phys Rev B*. 2008;77(10):104442.

66. Hollmann N, Hu Z, Willers T, et al. Local symmetry and magnetic anisotropy in multiferroic $MnWO_4$ and antiferro-magnetic $CoWO_4$ studied by soft x-ray absorption spectroscopy. *Phys Rev B*. 2010;82(18):184429.

67. Liu G, Liu Z, Chai Y, et al. Magnetic and electric field dependent anisotropic magnetoelectric multiferroicity in $SmMn_3Cr_4O_{12}$. *Phys Rev B*. 2021;104(5):054407.

68. Kuhl KP, Hatsukade T, Cave ER, Abram DN, Kibsgaard J, Jaramillo TF. Electrocatalytic conversion of carbon dioxide to methane and methanol on transition metal surfaces. *J Am Chem Soc*. 2014;136(40):14107-14113.

69. Liu S, Wang X-Z, Tao H, et al. Ultrathin 5-fold twinned sub-25 nm silver nanowires enable highly selective electroreduction of CO_2 to CO. *Nano Energy*. 2018;45: 456-462.

70. Liu S, Sun C, Xiao J, Luo J-L. Unraveling structure sensitivity in CO_2 electroreduction to near-unity CO on silver nanocubes. *ACS Catal*. 2020;10(5):3158-3163.

71. Li H, Wen P, Itanze DS, et al. Colloidal silver diphosphide (AgP_2) nanocrystals as low overpotential catalysts for CO_2 reduction to tunable syngas. *Nat Commun*. 2019;10:5724.

72. Xiao H, Cheng T, Goddard Iii WA. Atomistic mechanisms underlying selectivities in C_1 and C_2 products from electrochemical reduction of CO on Cu (111). *J Am Chem Soc*. 2017;139(1): 130-136.

73. Bagger A, Ju W, Varela AS, Strasser P, Rossmeisl J. Electrochemical CO_2 reduction: a classification problem. *ChemPhysChem*. 2017;18(22):3266-3273.

74. Peterson AA, Nørskov JK. Activity descriptors for CO_2 electroreduction to methane on transition-metal catalysts. *J Phys Chem Lett*. 2012;3(2):251-258.

SUPPORTING INFORMATION

Additional supporting information can be found online in the Supporting Information section at the end of this article.